MET.O.14

METEOROLOGICAL OFFICE
BOUNDARY LAYER RESEARCH BRANCH
TURBULENCE & DIFFUSION NOTE

T.D.N. No. 106

THREE-DIMENSIONAL NUMERICAL INTEGRATIONS OF THE NAVIER-STOKES EQUATIONS FOR FLOW OVER SURFACE-MOUNTED OBSTACLES

by

P.J.Mason & R.I.Sykes

August 1978

Final version 4/10/78

To appear JFM 91, pt 3, p433

AUG 1978

Three-dimensional numerical integrations of the Navier-Stokes equations for flow over surface-mounted obstacles

by P.J. Mason

& R.I. Sykes

Meteorological Office, Bracknell

Abstract

Numerical integrations of the Navier-Stokes equations for flow past a smooth, three-dimensional, surface-mounted obstacle are presented. The variation of the flow with Reynolds number, and with geometric ratios such as the maximum slope of the obstacle, are investigated. The separated flow is investigated using visualisations of the surface-stress patterns, and also particle trajectories through the flow.

1. Introduction

Fluid flow past three-dimensional surface-mounted bluff obstacles is a subject of considerable interest in many fields. In the widest context, atmospheric flow over bluff topography or buildings, flow over protuberances on aircraft or vehicles, and internal flows over obstacles in pipes and ducts all demand an understanding of the general phenomenon. Sedney (1973) presents a review of the subject, and indicates the complete lack of detailed knowledge of such flows. The principle difficulty is the problem of the measurement and visualisation of the enormous amount of information necessary to describe a complex three-dimensional flow. Hunt et al (1978) present a purely kinematical study intended as an aid to interpretation and comprchension of three-dimensional separated flows, underlining the shortcomings of experimental results; the data is often incomplete or ambiguous, and requires interpretation to give a complete description of the flow field. Except for the simplest geometrics, even the most general features such as separation lines may be unknown.

In many physical problems, numerical computation is used as a means of obtaining greater detail, complementing experimental results. The present speed and size of digital computers makes the numerical solution of some three-dimensional flow problems possible. In contrast to experimental methods, numerical solution of the equations of motion provides a complete description of the velocity field, but suffers stricter restrictions on the parameters and geometries which can be studied. In this paper, some numerical solutions of the Navier-Stokes equations for flow over surface-mounted obstacles with simple geometry and moderate Reynolds numbers are presented. If the results of this study are to correspond with the continuous solution of the differential

equations then, at the very least, the resolution of the finite difference model must always be finer than any scales of the continuous solution. It is this requirement which sets a limit to the Reynolds numbers for which a solution can be obtained. This computational requirement proves to be very stringent for objects with sharp corners, such as cubes, and the present work deals with smoothly shaped obstacles. It is hoped that the thorough flow visualisation obtained from these calculations will not only be of interest in its own right, but will also help clarify the mechanisms at work in more complex flows.

Before describing the numerical techniques and results, some general concepts of separated flows are worth considering. In two dimensions, separation is unambiguously defined by a streamline detaching from the surface, generating a closed circulation. Unfortunately, the situation is not so simple in three-dimensions. Separation at very large Reynolds number is identifiable by the boundary layer leaving the surface, but a useful definition of separation valid for all Reynolds numbers is not so obvious. Lighthill (1963) considers the singular points in the surface - stress field, ie the points where the vector tangential stress vanishes, and suggests that separation and attachment lines must begin and end in singular points. The nature of these points has been characterised in terms of 'nodes' and 'saddle points', applying topological principles to determine constraints on the possible streamline patterns (see eg Lighthill (1963), Hunt et al (1978)). These singular points are undoubtedly the most striking feature of a flow pattern when they are present, and we shall relate our numerical results to the recent results of Hunt et al (1978) where possible. However, singular points are shown not to be necessary for separation to

occur, and in section 4 we shall present an example of a separated flow without any singularities in the surface stress field.

It is, of course, difficult to discuss separation without a firm definition of the phenomenon. Throughout this paper, we use the term in an intuitive manner. By a separated flow in the context of surface-mounted obstacles, we mean a flow in which fluid particles originating close to the surface upstream can be transported some distance away from the surface. Thus, particle trajectories are used to determine whether the flow is separated. It may be possible, following Maskell (1955), to form a strict definition, based on the above, be defining 'close to the surface' as the limit as the point of origin of the particle approaches the surface. Then a separated flow would be one in which a particle originating arbitrarily close to the surface upstream, was displaced by a finite distance from the surface at some point on the trajectory. The definition could be made more general by removing the constraint that the point of origin be upstream, any point on the surface would suffice, allowing flow over free obstacles to be included. It is not clear whether this definition would contain all the known separations, since the detailed structure is only known in very simple cases. The point is not pursued here, since any definition involving such limits is impossible to apply strictly to a finite-difference solution, and is even more academic in experimental investigations.

2. Equations of motion and boundary conditions

The equations of motion governing the integrations reported in this paper are the Navier-Stokes equations for an incompressible, rotating fluid, ie

$$\frac{\partial \underset{\sim}{u}}{\partial t} + \underset{\sim}{u}.\nabla \underset{\sim}{u} = -\nabla p + 2\underset{\sim}{\Omega} \wedge \underset{\sim}{u} + \nu \nabla^2 \underset{\sim}{u} \qquad (1)$$

$$\nabla . \underset{\sim}{u} = 0 \qquad (2)$$

where $\underset{\sim}{u} = (u, v, w)$ is the velocity, p is the pressure, ν is the kinematic viscosity, and $\underset{\sim}{\Omega}$ is the basic rotation. As we shall see later, the basic rotation is dynamically negligible in the integrations to be presented. The Coriolis term, $2\underset{\sim}{\Omega} \wedge \underset{\sim}{u}$, is necessary to obtain a horizontally homogeneous boundary layer; this point is discussed below.

The geometry and coordinate system are illustrated in figure 1, showing the lower boundary defined by $z = h(x,y)$. The boundary conditions on the upper and lower surfaces are

$$\frac{\partial u}{\partial z} = \frac{\partial v}{\partial z} = w = 0 \quad \text{on} \quad z = D$$

$$\underset{\sim}{u} = 0 \quad \text{on} \quad z = h(x,y)$$

respectively. Thus the upper surface is a slippery, rigid lid, although this was located sufficiently far away to effectively simulate an infinite fluid in the integrations below.

In both horizontal directions, the domain of integration is taken to be periodic. The main reason for this choice, apart from its simplicity from the numerical aspects, is our interest in the total drag due to presence of a hump. The drag is composed of a pressure force on the obstacle together with the viscous stress on the surface.

The influence of the hump on the viscous stress may extend very far downstream, and is consequently very difficult to calculate accurately, unless the domain is self-contained as in the periodic case. The results of the force calculations are described in Mason and Sykes (1979), but since the integrations demand a great deal of computation it has proved impossible to calculate a similar range of flows without rotation. The basic rotation is necessary if periodic boundary conditions are specified, since a horizontally homogeneous background state is required. The Ekman boundary layer (see eg Greenspan 1968) satisfies this condition, but the direction of the velocity swings through 45° between the surface and the free stream. A non-rotating boundary layer grows in the downstream direction, thus periodicity is precluded.

Although it has some geophysical relevance, the non-parallel incident flow complicates the flow around the obstacle, and the periodic boundary conditions sometimes mingle upstream and downstream effects. Thus, a small number of integrations have been made using different boundary conditions in order to study parallel flow past an isolated obstacle. In these cases the rotation frequency $\Omega = 0$, and the Blasius boundary layer profile is used to define the velocity at the inflow boundary. A simple outflow condition, described in the next section, is specified at the outflow boundary, allowing disturbances to leave the domain.

For these integrations, in order to economise on computer resources, the flow is assumed to be symmetric about the centre line of the obstacle, $y = 0$. This may artificially stabilise the flow, eg by preventing time-dependent eddy shedding, but the results still serve their prime purpose of giving a clearer picture of the flow field. In the y-direction slippery, rigid walls are imposed, ie

$$\frac{\partial u}{\partial y} = \frac{\partial w}{\partial y} = v = 0 \quad \text{on} \quad y = 0 \text{ and } L_y$$

where L_y is the width of the integration domain.

3. Numerical method

The numerical techniques available for the solution of the Navier-Stokes equations on an orthogonal mesh of grid points are well-documented and plentiful. The most difficult aspect of the present work is the inclusion of an irregular lower boundary. The method used here is a crude but simple technique which allows the equations to be solved accurately on the normal Cartesian mesh, provided certain restrictions are met. A complete description of its application to two-dimensional flows is given in Mason and Sykes (1978), but a brief discussion is in order here.

A Cartesian mesh of grid points is defined, without regard to the position of the surface; thus a number of points in the domain of integration will be below the lower boundary, and consequently outside the physical domain. The velocity on all such non-physical points is maintained at zero throughout the integration. Derivatives involving points near the boundary must be considered separately, since the actual surface lies between grid points. The simplicity of the method is due to the fact that only the viscous term is modified near the surface. Whenever a viscous stress term, ie viscosity multiplying a velocity gradient, is calculated using velocity values from both sides of the boundary, a modified value of viscosity is used which ensures that the stress has the same value as the stress calculated assuming zero velocity on the surface. Figure 2 illustrates the situation when a vertical derivative of the x-component of velocity is being calculated. The grid length is Δ, so the stress calculated by the model is

$$\nu_{int}\,\frac{(u_Q - u_P)}{\Delta} \;=\; \nu_{int}\,\frac{u_Q}{\Delta}$$

since $u_P = 0$. ν_{int} is an interpolated viscosity value, chosen to

make the stress equal to $\nu u_q/(\Delta-\eta)$, which is the value obtained assuming $\underset{\sim}{u}$ vanishes on the surface. Thus

$$\nu_{int} = \nu \frac{\Delta}{\Delta-\eta}$$

Other components of the stress tensor are calculated analogously. Note that these approximations are only first order accurate, thus the error will be $O(\Delta/\lambda)$ where λ is the scale of variation of the stress. No attempt to modify the inertial term is made, thus the errors in this term will be $O(1)$. However, since the velocity vanishes on the surface, the inertial term is very small and is shown in Mason and Sykes (1978) to be $O(\Delta/\lambda)^2$ relative to the viscous term, hence the errors are also negligible.

The length scale of the stress variation, λ , is not simply the boundary layer depth, but must be obtained from a scale analysis of the dynamical equations. For the situation we are considering here, the balance near the surface must be between the inertial and the viscous terms. The stress has a magnitude of order $\nu u_o/\delta$ where u_o is the free stream velocity, and δ is the boundary layer depth. Hence the viscous stress gradient will be $\sim \nu u_o/\delta\lambda$. In the flows considered in this paper, all length scales will be of order δ , thus the inertial term within a distance of $O(\lambda)$ of the surface will be $\sim \lambda^2 u_o^2/\delta^3$, assuming $\lambda<\delta$, Thus equating the two magnitudes gives

$$\lambda = (\nu\delta^2/u_o)^{1/3} = \delta . Re^{-1/3}$$

where $Re = u_o\delta/\nu$, the Reynolds number of the boundary layer. This provides the restriction on the grid spacing which must be satisfied for this method to give accurate results. If a no-slip boundary is required, this method is not very restrictive, since the scale λ is

a dynamical scale near the surface which must be resolved in any model. The only problem with the Cartesian mesh is that the grid points must be distributed throughout the height of the obstacle rather than in a layer on the surface. However, in a separated flow, the resolution is required in the lee of the hump to resolve the shear layers there, therefore the grid points away from the obstacle are not wasted.

This Taylor series approximation for the terms near the boundary is not new, indeed some workers have also approximated the inertial terms by a similar technique. The novelty of the method used here is the ability to solve the Poisson equation for the pressure in the entire Cartesian domain, rather than the physical domain. It is shown in Mason and Sykes (1978) that pressure can be defined below the boundary in such a way that the continuity equation (2) is satisfied everywhere. This allows the use of fast numerical techniques for the solution of the elliptic equation, which, together with the fact that only the viscous term is modified near the surface, makes our method computationally very fast. The execution time is essentially the same as that for a Cartesian model with plane boundaries.

The basic model used in this work has a mesh of up to 40x40x32 points in the (x, y, z) - directions respectively, with the ability to stretch the grids in all three coordinate directions. Spatial difference are second-order accurate provided the mesh size does not change too rapidly (Kalnay de Rivas 1972), and the stretching allows grid points to be concentrated in the area of interest. The temporal derivative is approximated by the 'leapfrog' centred difference, and the inertial terms use the conservative form due to Piacsek and Williams (1970). Variables are stored on the usual staggered mesh, see eg Williams (1969). The viscous terms are in the Du Fort-Frankel form (see eg Potter, 1973), to avoid the unconditional instability associated with

the 'leapfrog' timestep. The Poisson equation is solved on the non-uniform grid by a direct method due to Farnell (1979). This method is an extension of the Fourier analysis technique, and uses eigenvectors of the finite difference operator to effect a direct solution in two of the directions. The final solution is then obtained by line inversion in the third direction. With a full mesh of grid points, the execution time is 8s per timestep on an IBM 360/195; this figure includes transfers between backup store and main core. The non-rotating model is identical in its formulation but has more flexibility in the number of grid points in each horizontal direction. The total number of points in a horizontal section must not exceed 1280, but may vary between 64x20, and 40x32 in the (x, y) - directions; the smaller number of points in the transverse direction being due to the transverse symmetry condition.

Finally, we describe the outflow condition in the non-rotating model. If the normal component of velocity at the outflow boundary is time-dependent, then an extrapolated value on the boundary must be set before the Poisson equation for pressure can be solved, and the velocity fields advanced. Sophisticated techniques are available to calculate the extrapolated value in a way which minimises the reflectivity of the boundary, eg Clark (1977). The extrapolation used here is extremely simple, but is stable and effective. We set

$$u_N^{t+1} = 1.5\, u_{N-1}^{t} - 0.5\, u_{N-3}^{t}$$

where the superscript denotes the time level, and the subscript denotes the x-coordinate. Thus the boundary value on the Nth point at the advanced time-level is a linear extrapolation using the current values on the adjacent interior grid point and the third point upstream. This extrapolation formula prevents the build-up of energy in grid-scale modes. Other velocity components are similarly extrapolated in space,

but need not be extrapolated in time, so all the quantities in the formula will be at the same time-level. This outflow condition was found to be stable but reflected some of the incident disturbance. Hence the temporal evolution of the flow was affected by the initial velocity field interacting with the outflow boundary. However, we are principly interested in the steady state solution, and the boundary condition does allow an arbitrary velocity profile at the outflow, thus the extreme complications necessary to achieve better transparency were not considered worthwhile here.

The fields used as the initial conditions for these integrations must be chosen to satisfy continuity. The Blasius profile as a function of distance from the flat boundary, $z = 0$, is set at each point above the physical boundary, $z = h(x,y)$. The x-components of velocity in each vertical column are then adjusted by the addition of a velocity independent of z, to give the same volume flux as that in the upstream profile. A vertical (w) velocity component is then calculated from continuity. This initial disturbance extends throughout the depth of the fluid, ie up to $z = D$, and has to be convected out of the domain before a steady solution can be achieved.

4. Results

All the integrations use a smooth obstacle with circular symmetry, and shape

$$h(x,y) = \begin{cases} h_0 \cos^2\left(\frac{\pi}{2a}(x^2+y^2)^{\frac{1}{2}}\right) & , x^2+y^2 \leq a^2 \\ 0 & , x^2+y^2 > a^2 \end{cases}$$

so h_0 is the maximum height, and a is the base radius. Any flow is effectively defined by three dimensionless numbers, viz a Reynolds

number, Re= $U_0\delta/\nu$, and two ratios of scales, h_0/δ and a/δ. As before, U_0 is the free-stream speed, and δ is the boundary layer depth. The Rossby number, Ro= $U_0 a/\Omega$, is strictly a fourth parameter, but in the integrations Ro is larger than 10, usually about 100, implying that the basic rotation plays no part in the dynamics of these flows. In all cases, the depth of the integration domain, D, is taken to be large enough to approximate to an infinite fluid. The computational efficiency of our model has enabled us to carry out enough integrations to study variations of all three independent parameters. Each integration was continued until the solution was steady, or until the initial transients had disappeared in the case of unsteady flows. This usually required about 1200 timesteps, representing an actual time of about $40a/U_0$.

Apart from cross-sections of velocity fields, two other methods of flow visualisation were employed. The surface stress pattern is displayed by calculating trajectories on a horizontal plane using the two horizontal components of tangential surface stress as the velocity field. A uniformly spaced array of 40x30 points in the horizontal plane was used as starting points for the trajectory calculations. From each point, trajectories were calculated numerically from the surface stress field, using a 4th order Kutta-Merson variable step technique (see eg Williams 1972). Values of the stress at intermediate points were linearly interpolated from grid point values. Trajectories were calculated both forward and backward for a short distance, which slightly randomises the end points of the lines. The resulting pictures are very similar to the oil-streak surface stress data obtained in experiments. The second display method is a perspective view of the three-dimensional trajectory of a fluid particle, calculated from the numerical velocity field. The integration and interpolation techniques are precisely the same as in the surface stress patterns.

We first present the results of our integrations of rotating flows, divided into sections describing the variation of each independent parameter. Finally, some data from non-rotating parallel incident flow integrations are described.

(a) Variation of Re

For the four integrations in this section, the geometric ratios are held constant at $h_0/\delta = a/\delta = 1$. A mesh of 40x32x32 points was used, with a grid spacing in the vicinity of the obstacle of about $h_0/10$. The free stream flow is in the x-direction from left to right in the diagram, implying the surface flow is at 45° as indicated by the bold arrows.

Figure 3 shows surface stress patterns from flows at four different Reynolds numbers. At the lowest Reynolds number, Re=20, which is illustrated in figure 3(a), the flow remains attached, although the surface stress vectors are clearly deflected over the hump. At Re=60, figure 3(b), separation is evident with reversed flow in the lee of the obstacle. This pattern exhibits the simplest combination of singularities, namely one node on the back slope, and one saddle point downstream, see eg Hunt et al (1978).

Increasing the Reynolds number to Re=200, figure 3(c), changes the character of the downstream separation. The enhanced reversed flow causes the nodel separation point in figure 3(b) to split in the transverse direction giving a separation line connecting a number of singularities, with the suggestion of a spiral node at one of the extremities. The length of the reversed flow region is also increased. Figure 3(c) also shows upstream separation, with flow near the surface diverging at the upstream saddle point, and reversed down the front-facing slope from the node.

Finally, figure 3(d) shows the surface stress pattern with Re=600. We must emphasise that this integration is strictly beyond the capabilities

of our numerical model. The restriction on grid length imposed by the requirement that the nonlinear energy cascade to short wavelengths be closed, ie that there is sufficient dissipation in the system, is not satisfied here. (This restriction is actually stronger than that implied by our method of including the curved boundary.) There is energy on the shortest scales in the numerical results with amplitude of about 20% of the maximum perturbation. This is principally due to the thin shear layer leaving the rear of the obstacle, and moving diagonally into the stretched mesh. The short waves have been numerically filtered in figure 3(d), therefore the results must be regarded with caution. The flow is not steady at this Reynolds number, and the separation line has clearly rolled up into vortices, which appear to break away downstream periodically. Figure 3(d) illustrates the surface stress pattern at $t=34a/u_0$, showing a vortex moving downstream on the upper half of the flow, with a new vortex forming on the rear slope of the obstacle. This is precisely as expected at higher Reynolds numbers as the separation lines become the edges of vortex sheets which will tend to roll up from the ends.

Information about the nature of the flow in the separated regions can be obtained from plotting particle trajectories. Figure 4 shows two perspective views illustrating the steady rear separation in the Re=200 case. The four trajectories originate at a height of $h_0/10$ above the surface upstream of the obstacle. Fluid approaching close to the base of the hump is deflected around the side, and then travels up the rear slope in the reversed flow. After reaching the separation lines, fluid particles move away from the surface almost horizontally, and clearly do not reattach downstream.

Figure 5 shows similar views of the upstream separation in the same flow. Flow attaches to the front slope at the upstream node in

figure 3(c). From this point particles spread over the surface of the obstacle. One of the trajectories moves back down the forward slope, then continues around the side and into the rear separation close to the surface. It finally separates there, and moves away downstream at a similar height to its point of origin. The other trajectories are deflected more simply over the summit and around the sides, where they separate from the upstream side of the separation line.

(b) Variation of h_o/a

In the integrations in this section, the Reynolds number Re=200, and $h_o/\delta = 1$, while the slope parameter h_o/a is varied.

Figure 6(a) shows the surface stress pattern when $h_o/a = 3$, while figure 6(b) is identical to figure 3(c), ie $h_o/a = 1$. The decrease in radius of the obstacle clearly restricts the separation line to a point, probably due to the decrease in Reynolds number based on the horizontal dimension. Figures 6(c) and 6(d) show the stress field with $h_o/a = 1/3$, and $h_o/a = 1/9$ respectively. The asymmetry of the flow is more pronounced at these parameter values, and the fluid is only entrained into the reversed flow region from one side only. An interesting feature of these flows is that there are no singularities associated with the separation line. Figure 7 shows trajectories for the case $h_o/a = 1/3$, clearly illustrating that the flow is indeed separated. Thus, the presence of singularities in the surface stress field are not necessary for the occurence of separation.

(c) Variation of h_o/δ

In this section, the Reynolds number Re=200, and $a/\delta = 1$. The results for increasing h_o/δ from $\frac{1}{4}$ up to 2 are shown in figure 8. It is clear that separation is becoming more violent as h_o/δ increases, in fact the instantaneous flow shown in figure 8(d) is very unsteady and strongly influenced by the periodic boundary conditions. However, it appears that the major

effects are due to the change in effective Reynolds number $R_h = U_h h_o / \nu$ where $U_h = \frac{1}{h_o} \int_o^{h_o} u_o(z)\, dz$ and $u_o(z)$ is upstream boundary layer profile. As h_o/δ decreases, the obstacle becomes submerged in the boundary layer, and the average velocity impinging on the obstacle is reduced. This must be borne in mind in the interpretation of figure 8.

(d) Parallel flow results.

Since the Ekman layer and periodic boundary conditions make the flow structure more difficult to interpret, a small number of integrations were performed using a non-rotating model with a Blasius boundary layer upstream. This allows both long itudinal and transverse cross-sections of the flow to be usefully examined. Whilst the gross features of the separation are visible in the previous integrations, the more subtle details of the work are impossible to distinguish. This is because the moderate Reynolds number implies that disturbances are damped fairly quickly downstream, therefore the trajectories are rapidly dominated by the streamwise velocity component, and appear straight. However, at higher Reynolds numbers, details of the secondary flow in the wake become much more pronounced. Features such as horseshoe vortices can dominate at high Re, producing spiral trajectories in the wake.

The boundary layer thickness, δ, is defined as the displacement thickness of the incident Blasius profile throughout this section. The first integration has Re=200, $h_o/\delta = 1$, and $a/\delta = 1/3$, so corresponds with the flow illustrated in figure 6(a). The surface stress pattern for the non-rotating flow is illustrated in figure 9, and has a similar structure to that of figure 6(a).

Figure 10 shows the velocity directions in the long itudinal section through the plane of symmetry, $y = 0$. These are produced in precisely the same manner as the surface stress patterns, using linear interpolation to obtain velocities between grid points. This is the cause of the slightly peculiar behaviour of the streamlines very close to

the surface. The position of the surface is only included via the viscous stress, so linear interpolation near the surface is not accurate. However, streamlines more remote than the nearest grid point to the surface are completely unaffected by this inaccuracy. Figure 10 clearly shows that the rear separation does not reattach but that fluid moves away horizontally downstream. Thus, in accord with Hunt et al (1978), both singularities upstream are attachment points, the pattern being almost symmetric about the centre of the obstacle.

Figure 11 shows a transverse cross-section just behind the hump The streamwise velocity component shows a slight shear layer associated with the separation. This diffuses very rapidly downstream. The secondary flow directions show two vortices outside the shear layer, one at the top in the centre and the other low down at the side. Both vortices rotate counter-clockwise. These are produced by the horseshoe vortex mechanism, ie upstream vortex lines being bent around the obstacle. From the surface stress pattern in figure 9, it can be seen that flow near the top of the obstacle flows around it, and flow near the surface is swept wide around the base. These two components appear to produce the two vortex centres in figure 11. Flow at intermediate levels upstream is entrained through the upstream separation into the rear separation, and thus emerges downstream on the inside of the shear layer. This part of the cross-section is dominated by the rising motion although a component of vorticity in the clockwise sense is visible.

The final integration is for Re=300, $h_0/\delta = 2$, and $a/\delta = 2$. This integration has a mesh of 64x20x32 points, and grid lengths in the vicinity of the obstacle are about $h_0/10$ again. The principal source of grid scale features in the similar flow in figure 6(d) was the fact that the shear layer did not remain within the region of fine grid. In the present integration, the grid length variations are below 10%, and the data presented contain no numerical smoothing. The flow is unsteady, with eddies travelling downstream and leaving the domain. The outflow condition does not seem to induce much upstream influence, and appears to transport the disturbances cleanly across the downstream

boundary. Unfortunately the imposed transverse symmetry almost certainly affects the dynamics of the eddy shedding; this must be borne in mind when interpreting the results. The rear separation, as illustrated by the surface stress pattern, shows the usual saddle point on the axis downstream of the obstacle splitting into a saddle on either side (only one side shown in the figure) and a node on the axis. The separation line clearly passes through a number of singularities, and is rolled up at its extremities. The surface stress pattern is relatively steady; the time-dependence is more obvious in the vertical sections presented below.

Figure 13 is a transverse cross-section immediately downstream of the obstacle, showing that the shear layer is much thinner than that in the previous flow. It is resolved by about three points at its narrowest section. The horseshoe vortex outside the shear layer is much stronger than in the previous flow, and has only one centre of rotation.

Figure 14 shows the streamlines in the long itudinal section through the centre-plane, $y = 0$, at a sequence of five different times.

The most striking feature of figure 14 is the rolling up of the flow leaving the top of the obstacle. As might be expected, the thin shear layer is not very stable, and temporal variations seem to be due to "flapping" of this vortex sheet. The sequence of streamlines shows swirls in the velocity field being generated immediately downstream of the obstacle, where the shear layer is thinnest, and travelling downstream and decaying. This eddy shedding is a regular phenomenon, and the Strouhal number, $\omega a / U = 1$. ω is the frequency of the eddy shedding. The change in the downstream surface singularity from a simple saddle point is further envinced in this vertical section. The pattern of the upstream separation has also changed, developing an apparently closed circulation. It is impossible to determine whether the streamlines are actually closed, since the results are numerical, but it is clear that there is a singularity away from the surface.

Returning to the spiral nodes associated with the downstream shear layer, figure 15 shows the longitudinal section of the streamwise velocity component. The shear layer leaving the back of the obstacle can be clearly seen. The dramatic spiralling flow visible in the streamlines is associated with minor perturbations of the shear layer; there is no rolling up of the shear layer itself.

Conclusions

The numerical integrations of flow around a surface-mounted obstacle have demonstrated a number of features of three dimensional separation.

Firstly, there are no closed stream surfaces in any of the flows presented here. The separating streamline does not reattach on the surface, but remains at some finite height downstream.

Singularities in the surface stress field are not a necessary condition for separation. A separation line can begin with a simple convergence of the limiting surface trajectories, and end with a cessation of that convergence.

In the integrations we have performed, it appears that Reynolds numbers of about 500 were necessary for the rolling up of streamlines to occur. This is a characteristic feature of high Reynolds number flows, with spiral nodes in the surface stress patterns, and also in fluid trajectories.

The results presented here demonstrate the utility of this numerical method in the study of flow over obstacles. With the number of grid points available in the work reported here, there is an upper bound on the Reynolds number of about 500. This restriction on Reynolds number is not basically due to the method of representation of the irregular lower boundary, but results from the more general requirement that small scale flow features are adequately resolved.

Acknowledgement

We would like to thank Miss P Ward for the development of the programmes to produce the three dimensional perspective views of the trajectories.

REFERENCES

Clark, T.L. (1977) 'A three-dimensional small scale dynamic model using a terrain-following coordinate transformation'. J Comp Phys. 24 p 186

Farnell, L. (1979) 'Solution of Poisson equation on a non-uniform grid' submitted to J Comp Phys.

Greenspan, H.P. (1968) 'The theory of rotating fluids'. Cambridge University Press.

Hunt, J.C.R., Abell, C.J. Peterka, J.A., & Woo, H. (1978) 'Kinematical studies of the flow around free or surface-mounted obstacles; applying topology to flow visualisation'. J Fluid Mech. 86 p 179

Kalnay de Rivas, E (1972) 'On the use of nonuniform grids in finite-difference equations'. J Comp Phys. 10 p 202

Lighthill, M.J. (1963) Laminar Boundary Layers. Oxford University Press. Ed. L Rosenhead

Mason, P J & Sykes, R.I. (1978) 'A simple Cartesian model of boundary layer flow over topography'. To appear in J Comp Phys.

Mason, P.J. & Sykes, R.I. (1979) 'On the net forces produced by surface-mounted obstacles'. To appear in Quart J Roy Met Soc.

Maskell, E.C. (1955) 'Flow separation in three dimensions Rep. aero. Res. Coun., Land. No 18063

Piacsek, S.A. & Williams, G.P (1970) 'Convservation properties of convection difference schemes'. J Comp Phys 6 p 392

Potter, D. (1973) 'Computational Physics'. Wiley

Sedney, R. (1973) 'A survey of the effects of small protuberances on boundary layer flows'. A.I.A.A. Journal 11 p 782.

Williams, G.P. (1969) 'Numerical integration of the three-dimensional Navier-Stokes equations for incompressible flow'. J Fluid Mech. 37 p 727

Williams, P.W. (1972) 'Numerical Computation'. Nelson, New York.

LEGENDS

Figure 1 — Schematic diagram of domain of integration.

Figure 2 — Illustrating the intersection of the curved boundary and a line of grid points.

Figure 3 — Variation of surface stress pattern for Ekman boundary layer flow with Reynolds number; (a) Re= 20, (b) Re = 60, (c) Re = 200 and (d) Re = 600.

Figure 4 — Two perspective views of particle trajectories illustrating the rear separation flow in the case Re = 200.

Figure 5 — Two perspective views of particle trajectories illustrating the upstream separation flow in the case Re = 200.

Figure 6 — Variation of surface stress pattern with h_o/a for Re = 200; (a) $h_o/a = 3$, (b) $h_o/a = 1$, (c) $h_o/a = \frac{1}{3}$, (d) $h_o/a = 1/9$

Figure 7 — Two perspective views of particle trajectories illustrating the rear separation flow in the case Re = 200, $h_o/a = \frac{1}{3}$.

Figure 8 — Variation of surface stress pattern with h_o/δ; (a) $h_o/\delta = \frac{1}{4}$ (b) $h_o/\delta = \frac{1}{2}$, (c) $h_o/\delta = 1$, (d) $h_o/\delta = 2$. The effective Reynolds numbers (see text) are R_h = 6, 24, 100, and 300 respectively.

Figure 9 — Surface stress pattern for parallel flow integration with Re = 200, $h_o/\delta = 1$ and $h_o/a = 3$.

Figure 10 — Long—itudinal (streamwise) section showing velocity directions in the centre plane for the flow shown in Figure 9.

Figure 11 — Transverse sections taken at the downstream extemity of the obstacle for the flow shown in Figure 9. (a) shows contours of the streamise velocity component and (b) secondary flow directions. The velocity contour values refer to a dimensionless free stream speed of 10. The vertical scale is plotted with a uniform grid spacing; the actual grid point coordinates are indicated by the arbitrary height scale on which h_o has value 1000.

Figure 12 — Surface stress pattern for parallel flow integration with Re = 300, $h_o/\delta = 2$, $h_o/a = 1$.

Figure 13 — Transverse sections taken at the downstream extremity of the obstacle for the flow shown in Figure 12. (a) shows contours of the streamwise velocity component and (b) secondary flow directions. The arbitrary scales are as with Figure 11.

Figure 14 — Long itudinal (streamwise) sections showing velocity directions in the centre plane for the flow shown in Figure 12 at different times. The dimensionless times, in units of a/U_o are (a) 68.9, (b) 70.5, (c) 72.1, (d) 73.7, (e) 75.3.

Figure 15 — Long itudinal (streamwise) section showing contours of the streamwise velocity component for the flow shown in Figure 12.

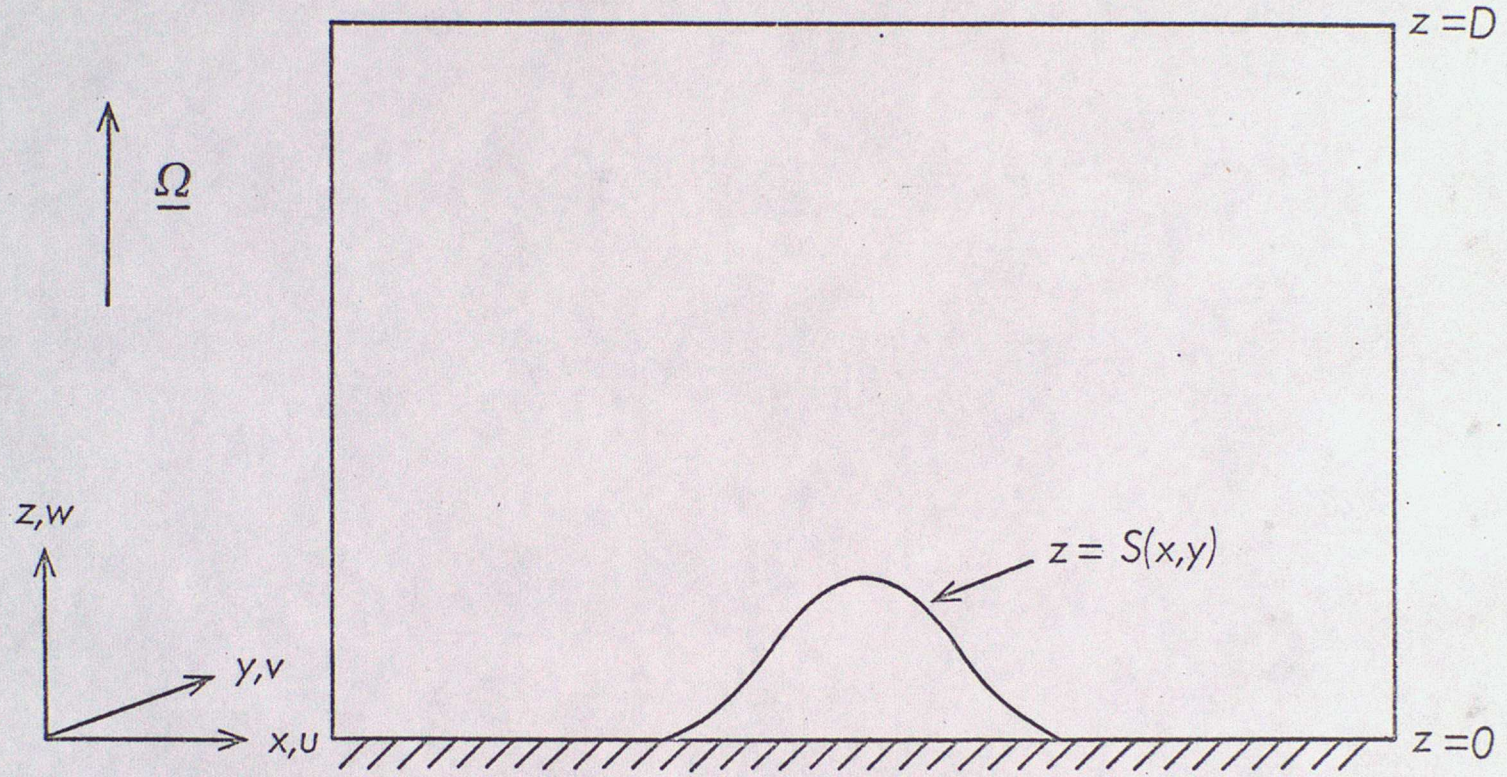

Figure 1

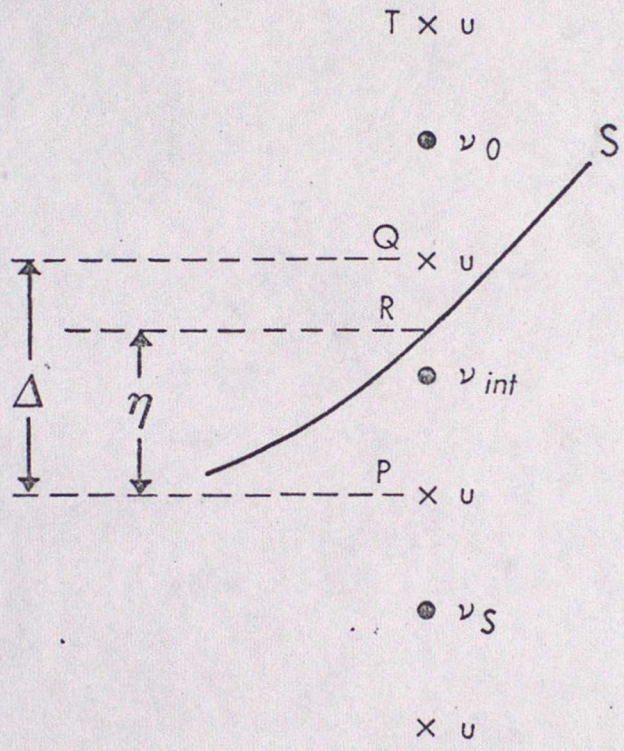

Figure 2

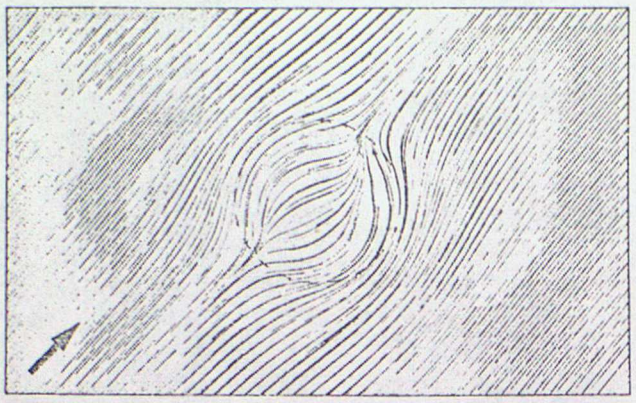

a

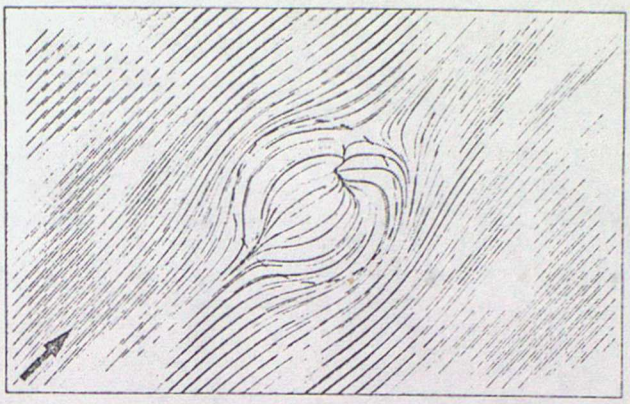

b

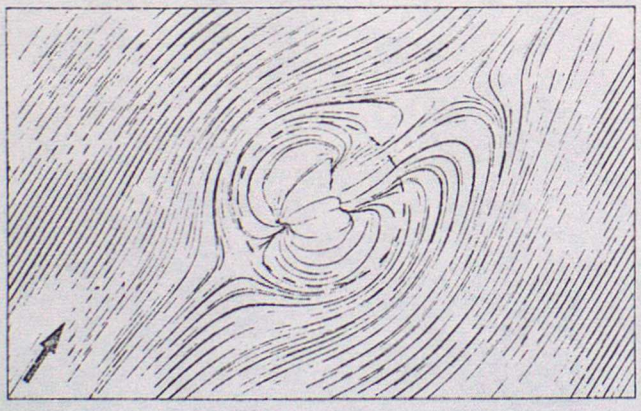

c

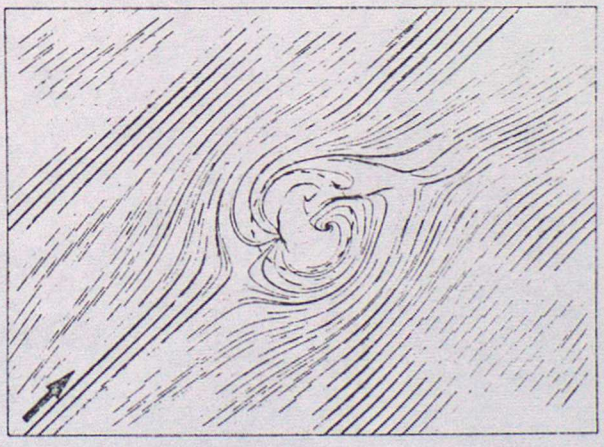

d

Fig 3

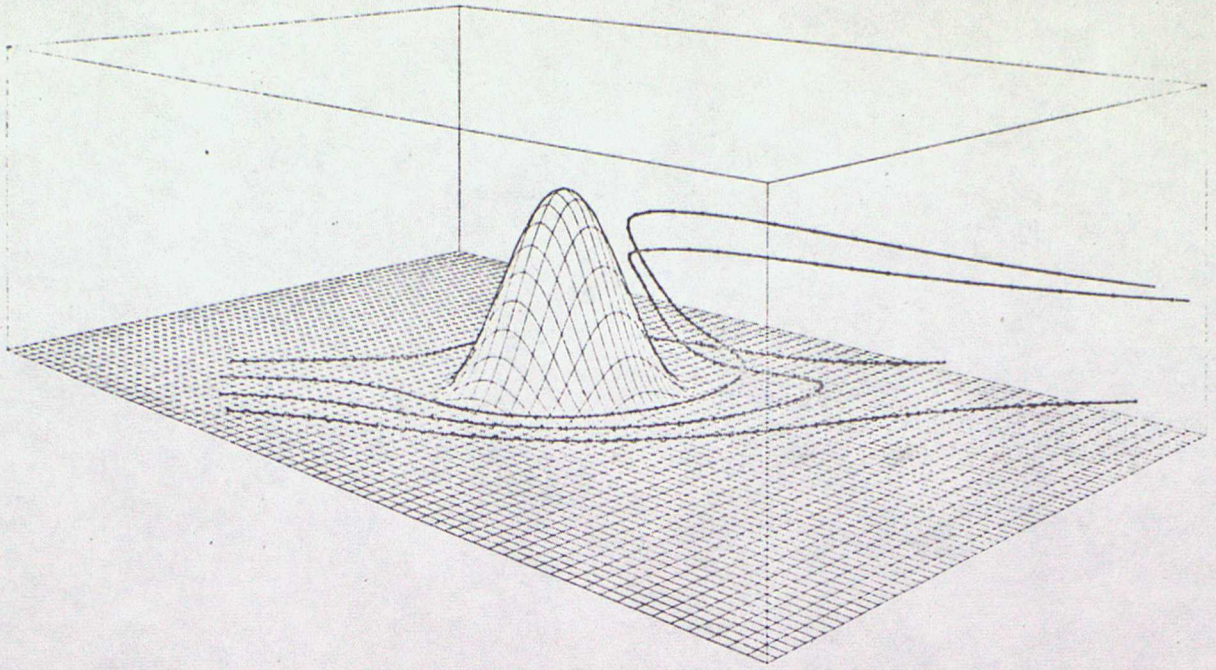

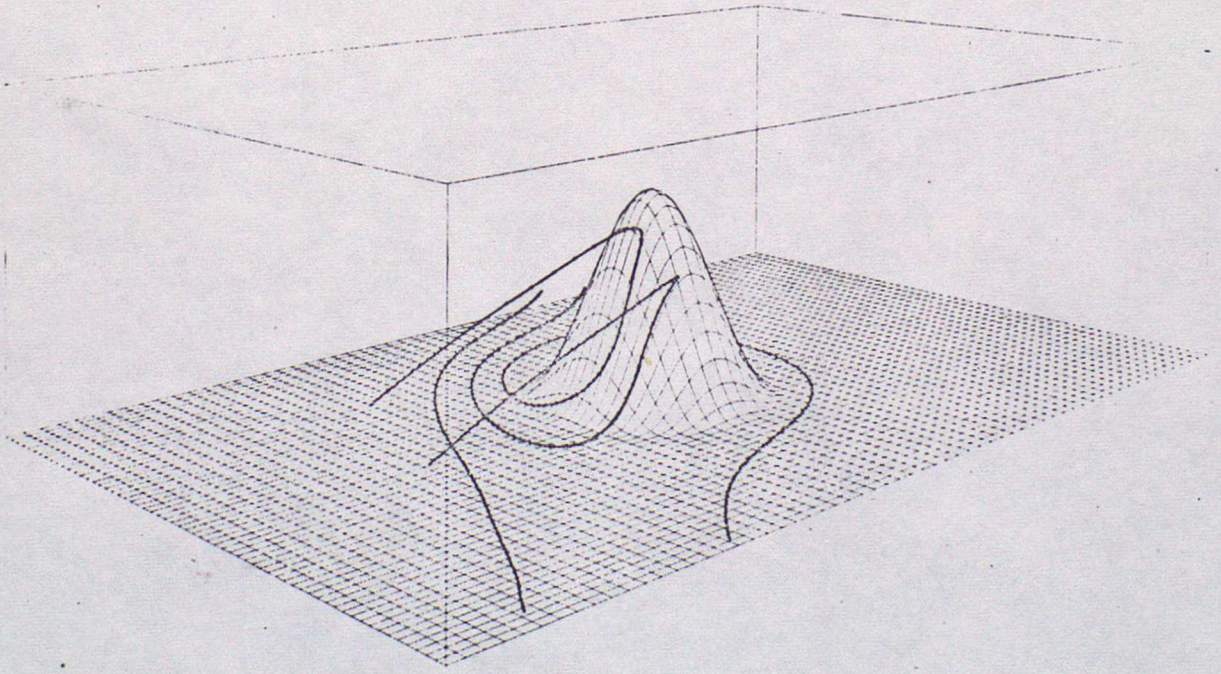

Fig 4

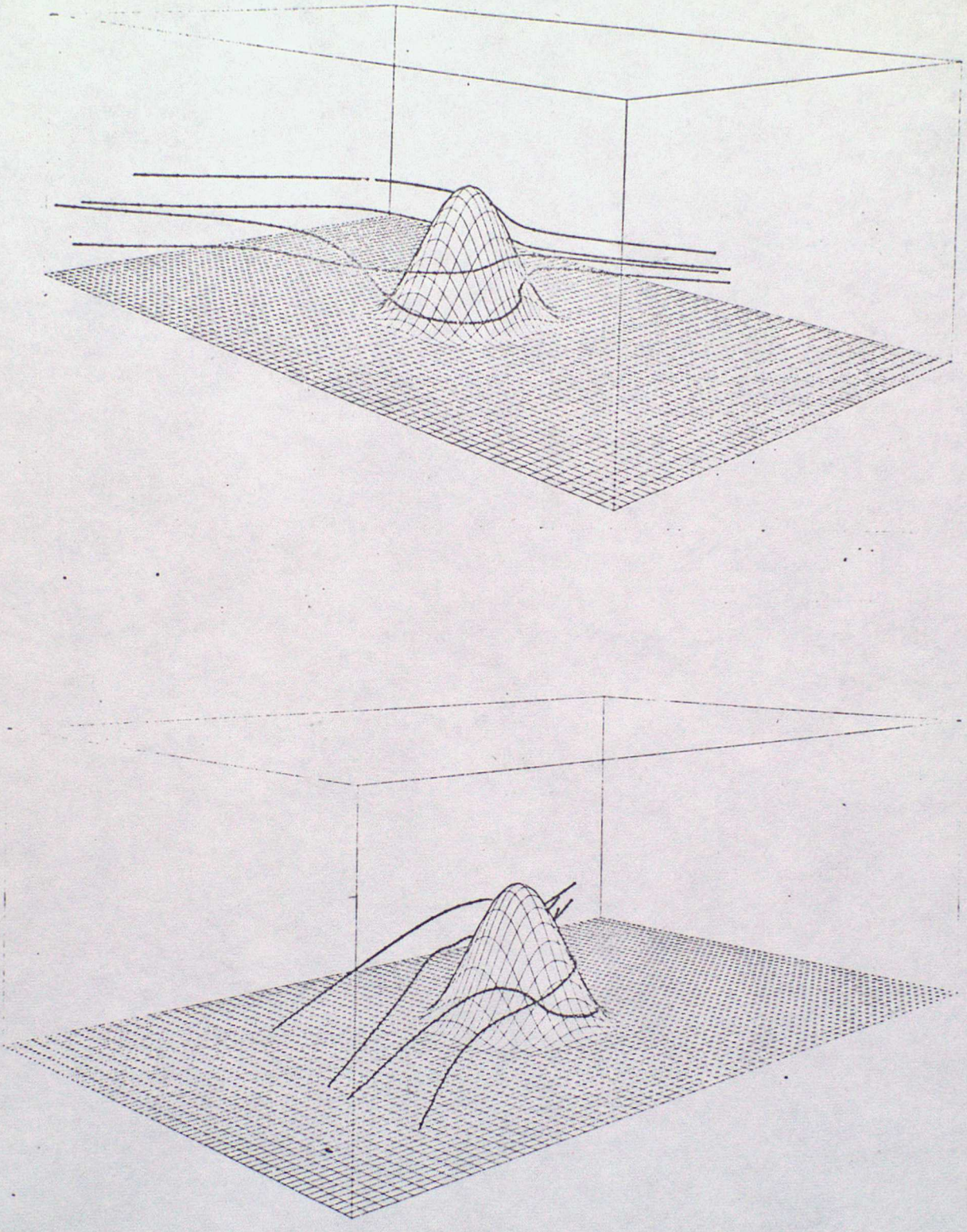

Fig. 5

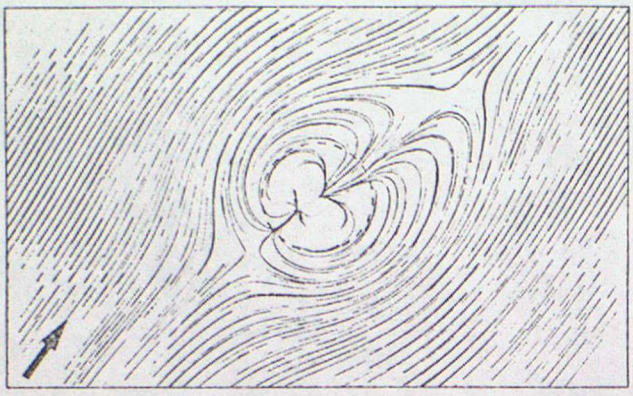

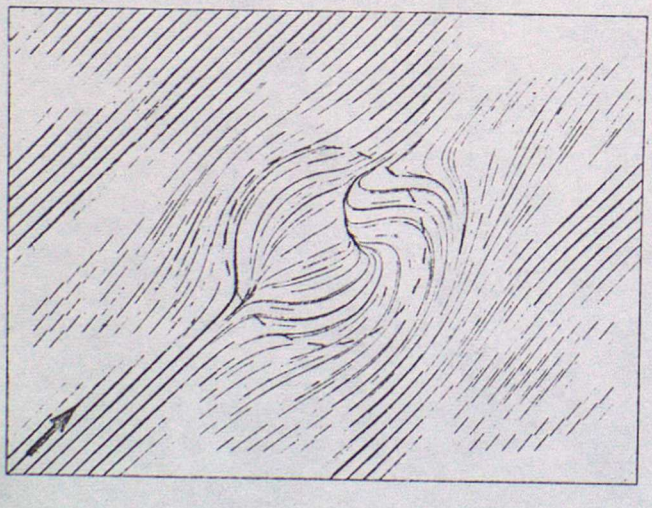

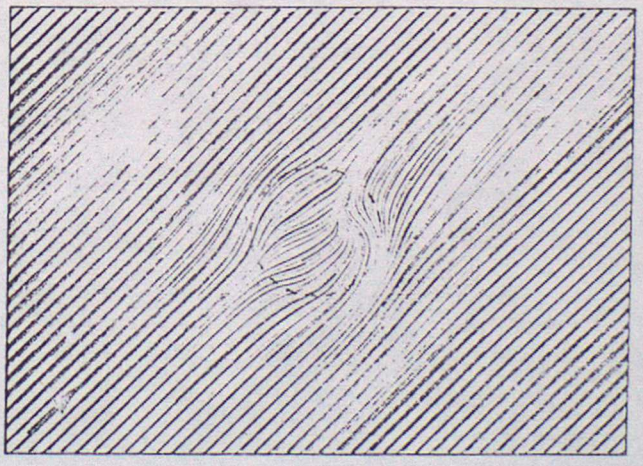

Fig. 6

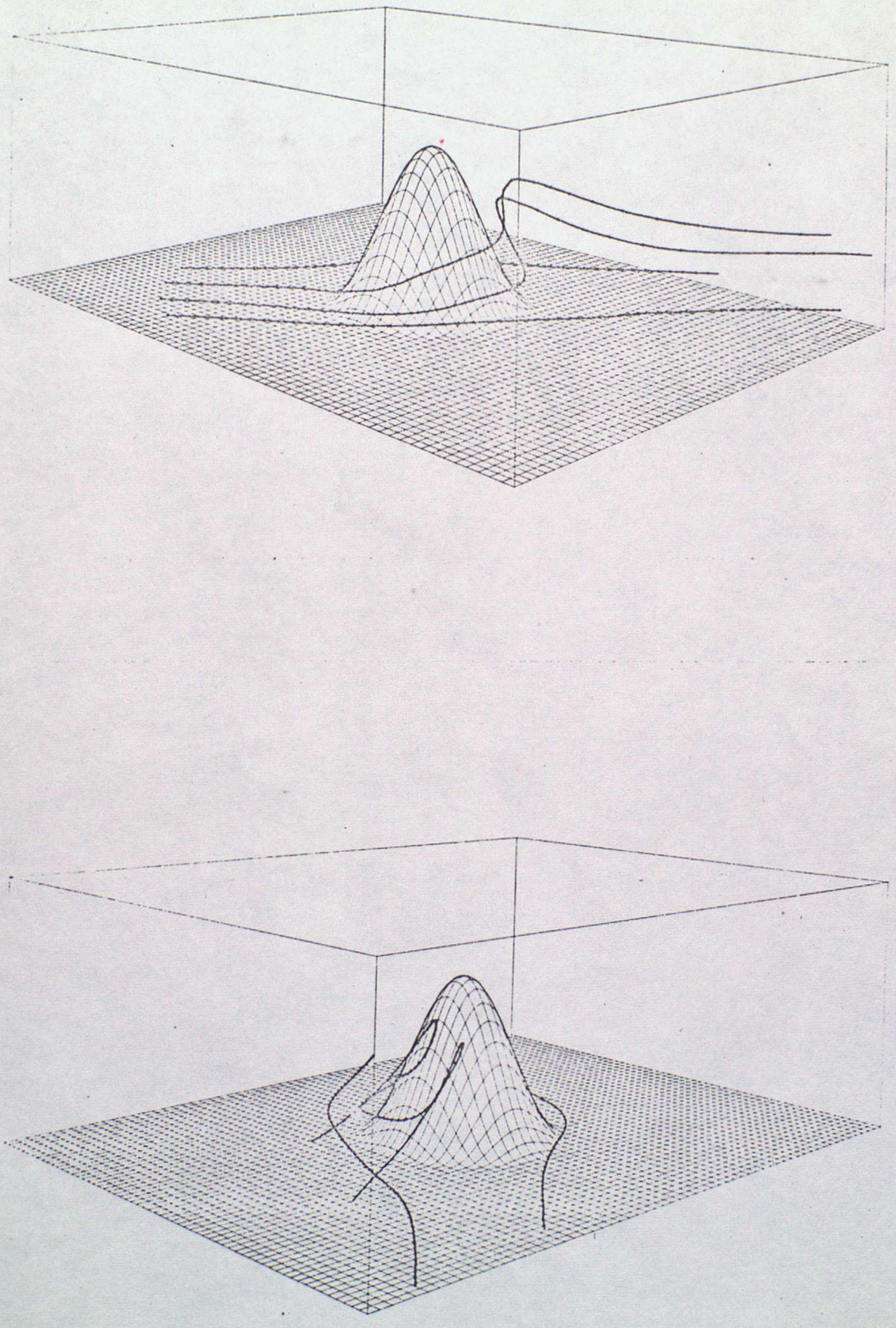

Fig. 7

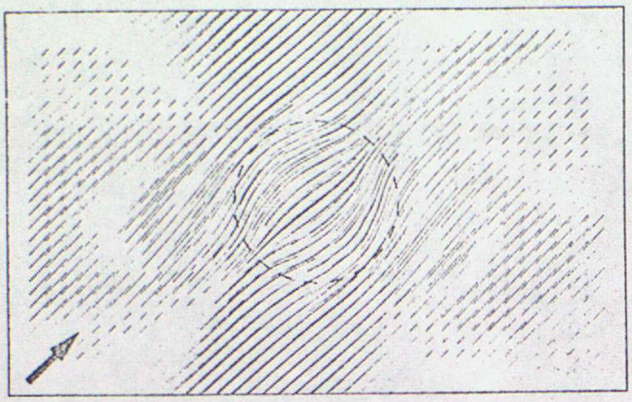

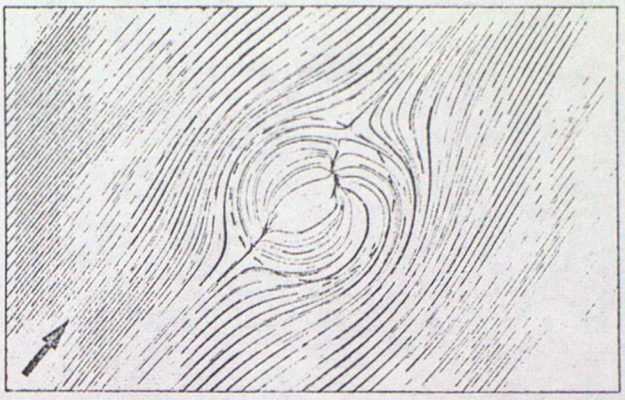

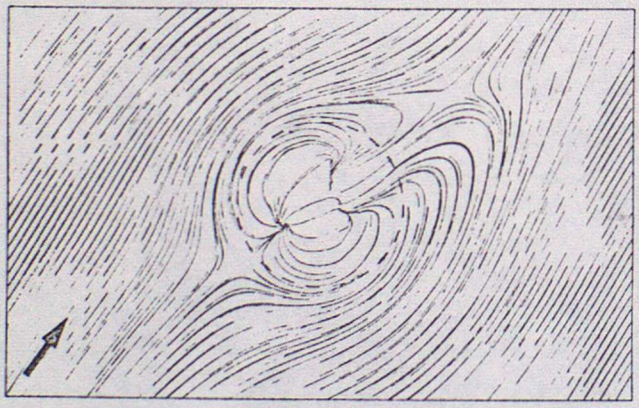

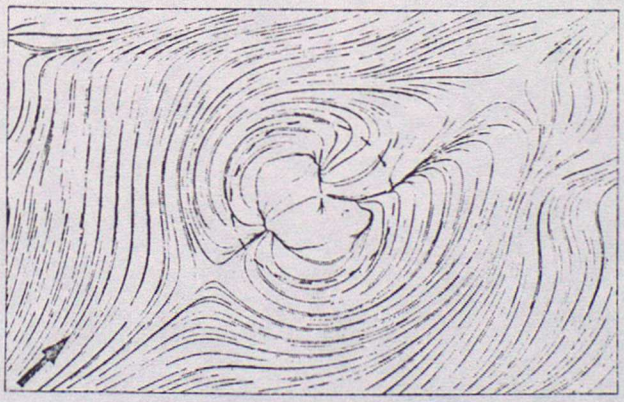

Fig. 8

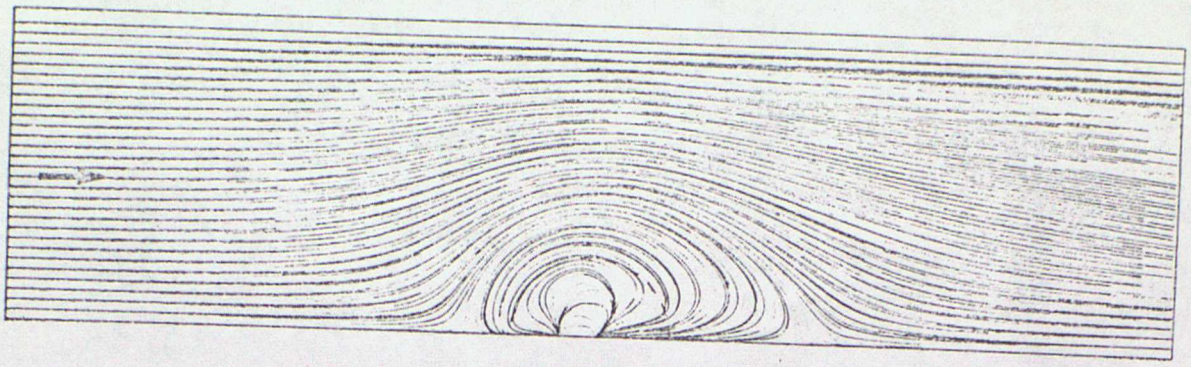

Fig. 9

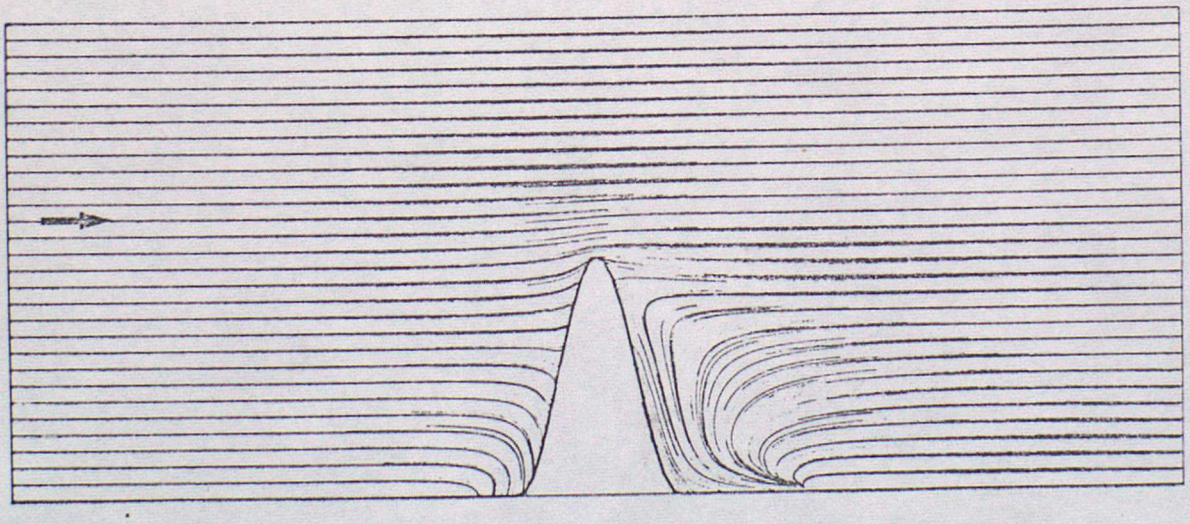

Fig 10

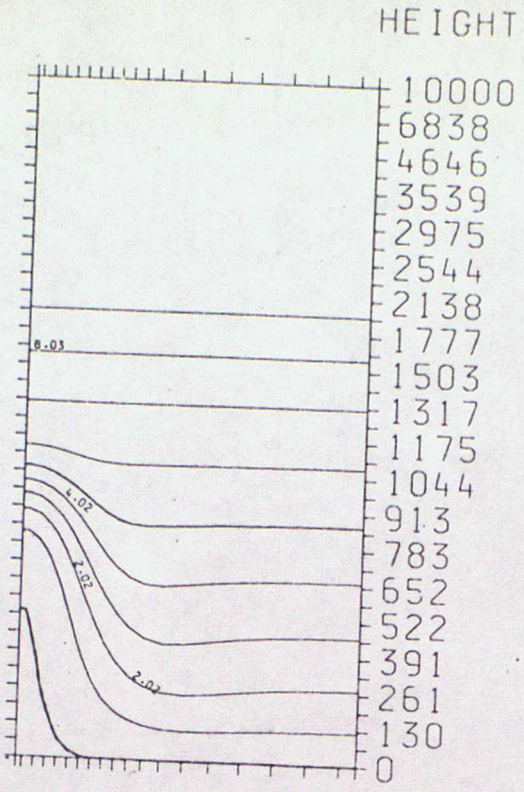

Fig 11 (a)

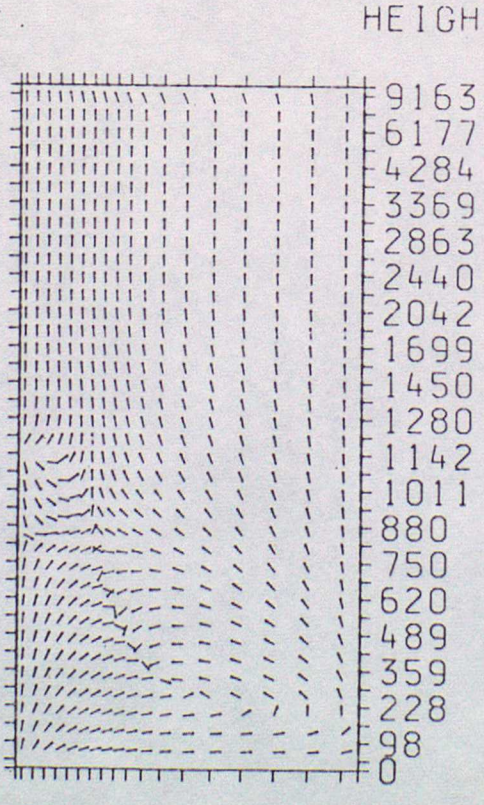

Fig. 11 (b)

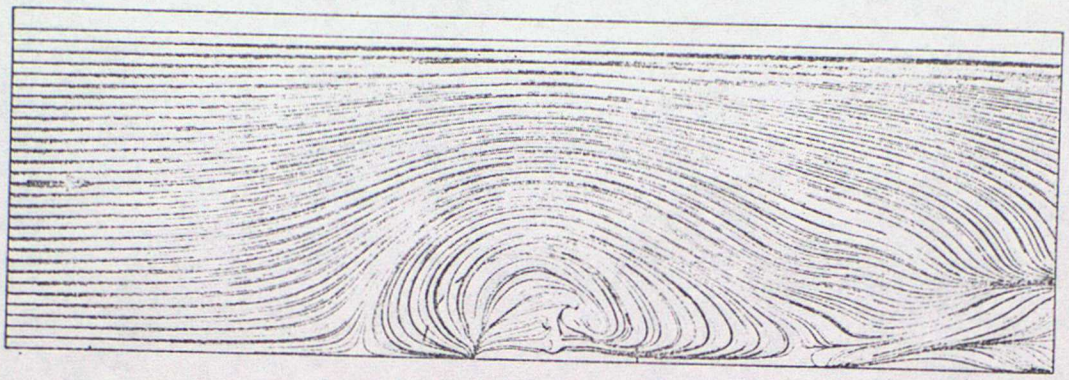

Fig. 12

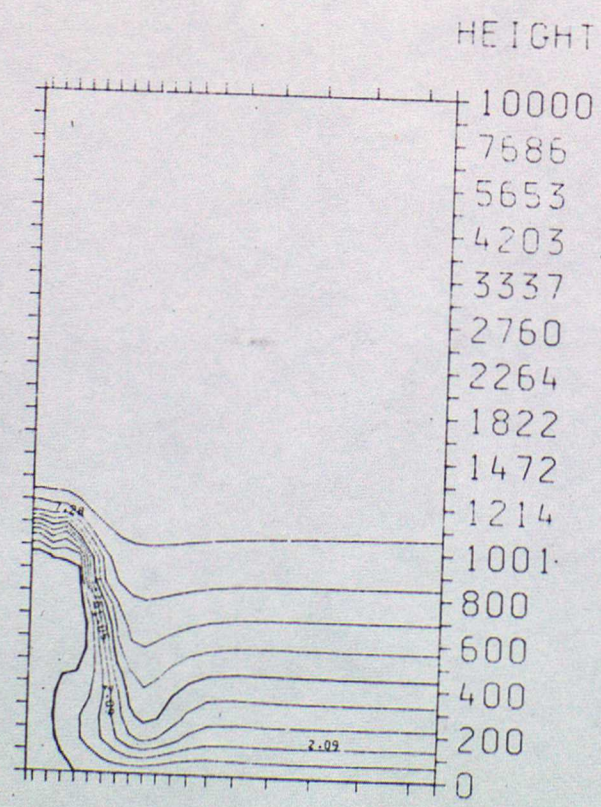

Fig. 13(a)

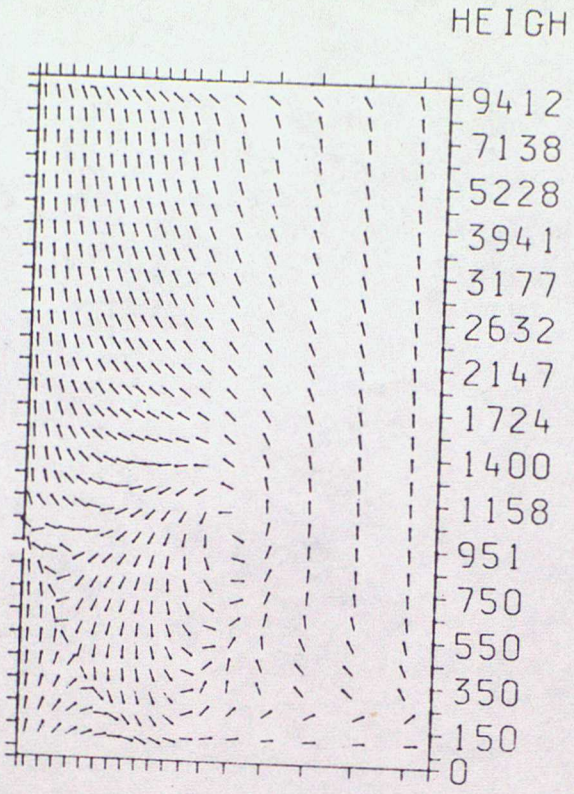
HEIGHTS
9412
7138
5228
3941
3177
2632
2147
1724
1400
1158
951
750
550
350
150
0

Fig. 13(b)

(a)

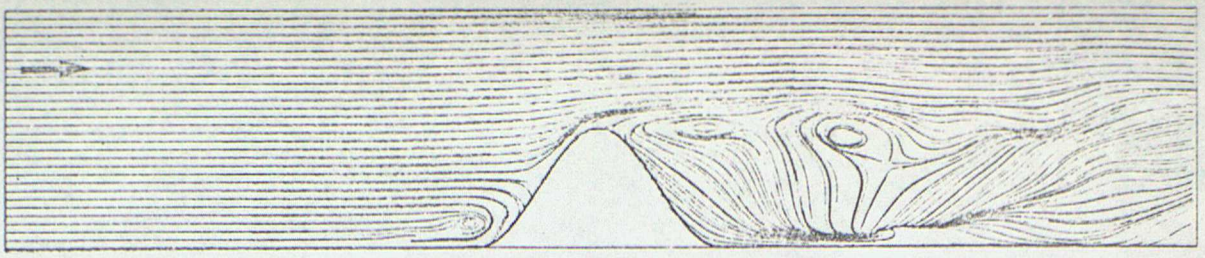

(b)

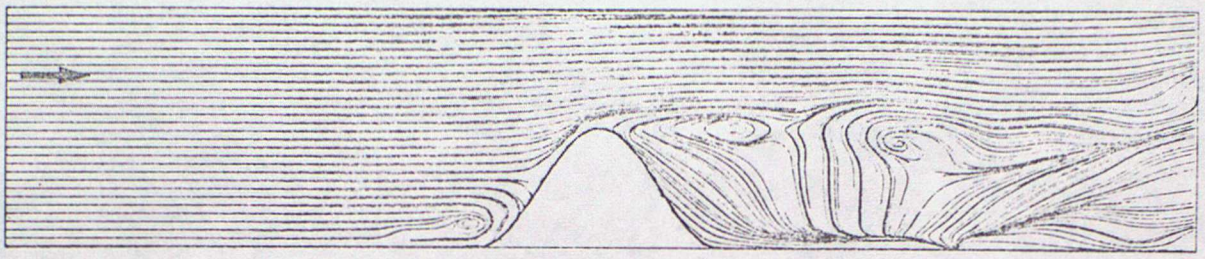

(c)

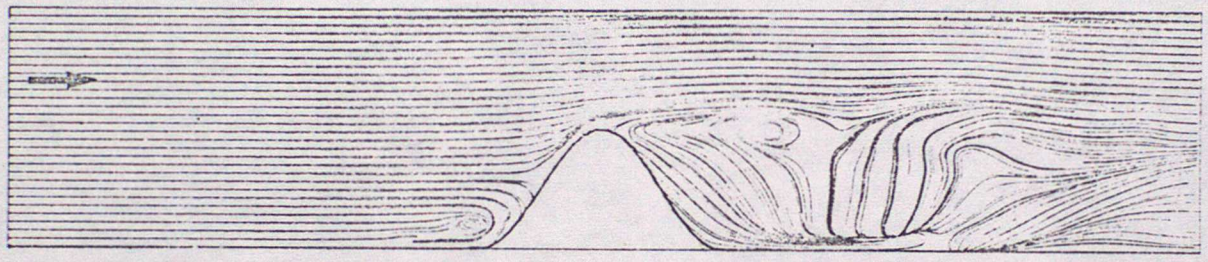

(d)

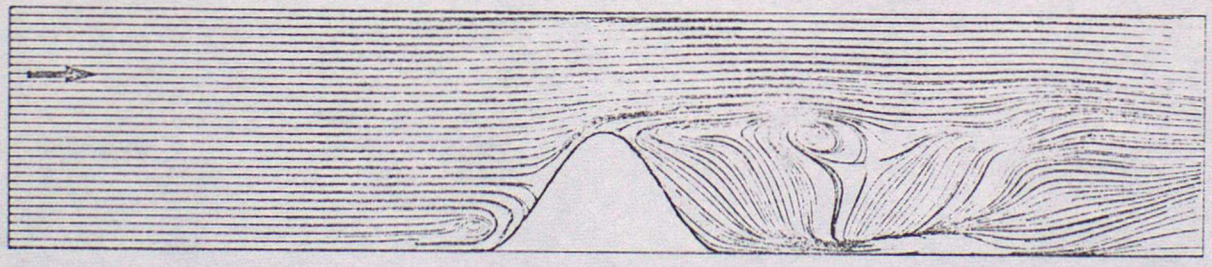

(e)

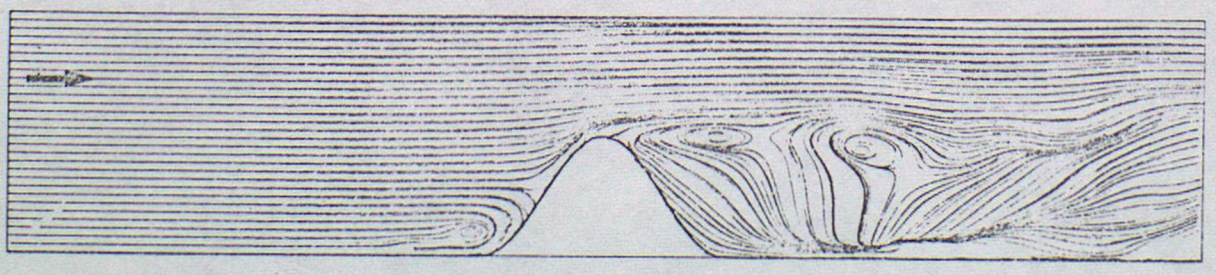

Fig. 14

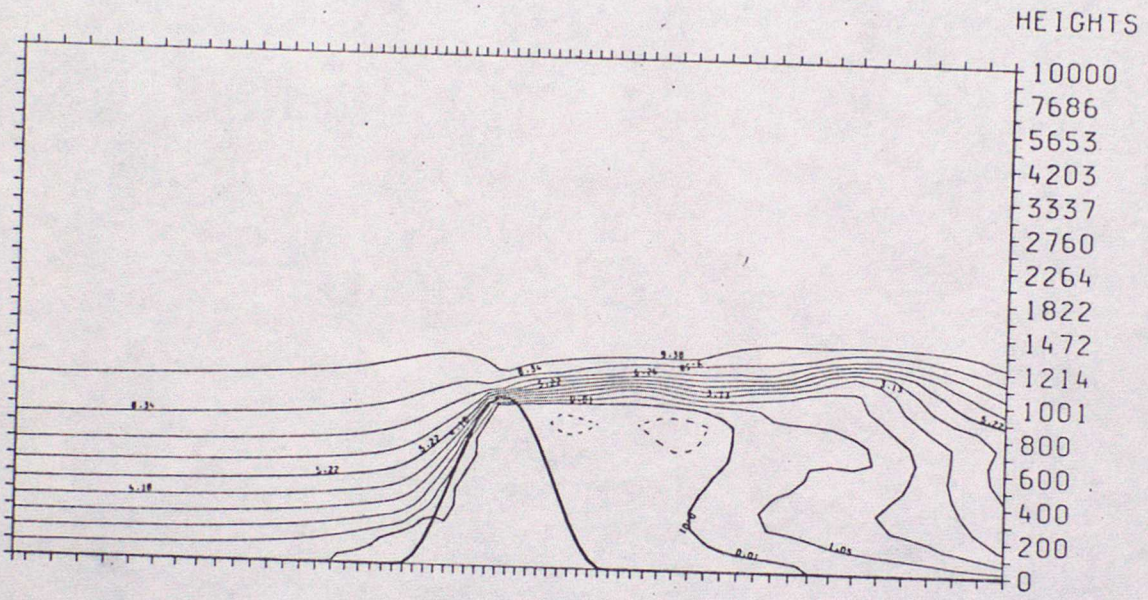
HEIGHTS
10000
7686
5653
4203
3337
2760
2264
1822
1472
1214
1001
800
600
400
200
0

Fig. 15